



Are Solar Active Regions Born with Neutralized Currents?

Aiying Duan^{1,2,3}, Yaoyu Xing¹, and Chaowei Jiang⁴

¹ Planetary Environmental and Astrobiological Research Laboratory (PEARL), School of Atmospheric Sciences, Sun Yat-sen University, Zhuhai 519000, China; duanaiy@mail.sysu.edu.cn

² Yunnan Key Laboratory of the Solar Physics and Space Science, Kunming 650216, China

³ Key Laboratory of Tropical Atmosphere-Ocean System, Sun Yat-sen University, Ministry of Education, Zhuhai 519000, China

⁴ Institute of Space Science and Applied Technology, Harbin Institute of Technology, Shenzhen 518055, China

Received 2024 April 17; revised 2024 May 6; accepted 2024 May 17; published 2024 July 1

Abstract

Solar active regions (ARs) are formed by the emergence of current-carrying magnetic flux tubes from below the photosphere. Although for an isolated flux tube the direct and return currents flowing along the tube should balance with each other, it remains controversial whether such a neutralization of currents is also maintained during the emergence process. Here we present a systematic survey of the degrees of the current neutralization in a large sample of flux-emerging ARs which appeared on the solar disk around the central meridian from 2010 to 2022. The vector magnetograms taken by Helioseismic and Magnetic Imager onboard Solar Dynamic Observatory are employed to calculate the distributions of the vertical current density at the photosphere. Focusing on the main phase of flux emergence, i.e., the phase in which the total unsigned magnetic flux is continuously increased, we statistically examined the ratios of direct to return currents in all the ARs. Such a large-sample statistical study suggests that most of the ARs were born with currents close to neutralization. The degree of current neutralization seems to be not affected by the active-region size, the active-region growing rate, and the total unsigned current. The only correlation of significance as found is that the stronger the magnetic field nonpotentiality is, the further the AR deviates from current neutrality, which supports previous event studies that eruption-productive ARs often have non-neutralized currents.

Key words: Sun: magnetic fields – Sun: flares – Sun: corona – Sun: coronal mass ejections (CMEs)

1. Introduction

It is commonly believed that solar active regions (ARs) are formed as magnetic flux thin tubes, which are generated and intensified in the convection zone, emerge into the atmosphere. Observations from photospheric vector magnetograms suggest that the emerging flux tube carries electric currents, and such current-carrying emerging flux from the solar interior is believed to be the main mechanism for forming the AR currents (Leka et al. 1996). Theoretically, the current flows in a coherent magnetic flux tube isolated with other magnetic fields (i.e., there is a field-free plasma surrounding the tube) consists of two parts: a direct current (DC) and a return current (RC) (Melrose 1991; Parker 1996; Török et al. 2014). DC is generated due to the twist and shear of the magnetic flux tube, and it is a volume current and often concentrates in the central part of the flux tube. On the other hand, the RC is a surface current which flows enveloping the DC with an inverse direction, and it isolates the flux tube from the ambient field by inducing a magnetic field that cancels the DC-induced field outside of the tube (Parker 1979). As this flux tube crosses through the photosphere, it is naturally inferred that the photospheric currents should be neutralized, that is, the DC and RC are balanced within each magnetic polarity of a simply

connected AR, as each polarity represents a cross section of the emerging flux tube of a Ω shape. It is further conjectured that a whole AR, which may have complex polarity distributions, also has no net current (i.e., the sum of all DCs and RCs), as the AR magnetic fields are composed of individual current-neutralized flux tubes (Parker 1979, 1996).

On the other hand, Melrose (1991, 1995) argued that as the magnetic flux emerges from the solar interior to form an AR, the RCs could escape detection and give rise to non-zero net currents. This is supported by some analytical modeling and numerical simulation. For example, based on an analytical model, Longcope & Welsch (2000) suggested that most of the RCs are trapped beneath the photosphere as magnetically isolated flux tubes emerge. Furthermore, Török et al. (2014) performed a three-dimensional magnetohydrodynamic (MHD) simulation of the emergence of a initially current-neutralized magnetic flux tube from below the photosphere. They found that the flux emergence creates a new flux rope in the corona, and the RCs resided at the top of the flux rope were pushed aside by subjacent DCs during the emergence, and some of the RCs short-circuit with adjacent DCs. These two processes give rise to coronal flux rope with a strong deviation from current-neutralization.

Therefore, it remains controversial on the current neutralization. Whether the currents are neutralized in solar ARs is not only relevant to the AR birth process, but also important for understanding the initiation mechanisms of solar eruptions. This is because solar eruptions, including solar flares and coronal mass ejections (CMEs), are powered by the free magnetic energy which can only be stored in coronal electric currents in ARs (Melrose 1991; Schrijver et al. 2005; Toriumi & Wang 2019). Many theories of eruption initiation tend to favor non-neutralization of the currents, for example, the ideal MHD instability models (Török et al. 2004; Kliem & Török 2006; Aulanier et al. 2010) which are based on a pre-eruption magnetic flux rope with a dominant DC along the axis of the rope. Some numerical simulations of CMEs (Török & Kliem 2005; Manchester et al. 2008) and coronal magnetic field reconstruction methods (van Ballegoijen 2004) are also based on the flux rope with non-zero net currents.

In observations, only two studies found that the photospheric current from an isolated sunspot is close to neutrality (Wilkinson et al. 1992; Venkatakrishnan & Tiwari 2009). Other studies have shown that the RC vanishes, namely, the net current is not zero in the photosphere (e.g., Leka et al. 1996; Longcope & Welsch 2000; Wheatland 2000; Ravindra et al. 2011; Georgoulis et al. 2012; Vemareddy et al. 2015; Liu et al. 2017; Vemareddy 2019; Avallone & Sun 2020; Fursyak et al. 2020). For example, Ravindra et al. (2011) analyzed the net currents in both the positive and negative polarities of AR NOAA 10930, and found that the net current in each polarity increased simultaneously with the flux emergence. Vemareddy et al. (2015) investigated the evolution of the net current in AR NOAA 11158, and explained the net current as an inevitable product of the emergence of a twisted flux rope. Furthermore, Vemareddy (2019) examined the current neutrality in five emerging ARs, and showed that the net current appears with the onset of the fast flux emergence and decreases to zero during the separation motion of bipolar regions. Some observations showed that pre-eruption ARs contain substantially non-neutralized currents, and found a close connection between the flare-CME eruption and the degree of net current neutralization as well. For example, Kontogiannis et al. (2017) compared the net currents in ARs with or without flares, and found that the average values of net currents in flaring ARs are one order of magnitude larger than those in non-flaring ARs. Both Liu et al. (2017) and Avallone & Sun (2020) suggested that the eruption productivity of an AR may be inversely related to its degree of current neutralization. Vemareddy (2019) also found that the ratio of DC to RC evolves to a higher level in CME productive ARs, while in flaring and quiet ARs it varies near unity.

In this paper, we carried out a systematic survey of the current neutralization in a large number of flux-emerging ARs, by employing the vector magnetograms taken by Helioseismic and Magnetic Imager (HMI, Hoeksema et al. 2014) onboard

Solar Dynamic Observatory (SDO, Pesnell et al. 2012) to calculate the distributions of the vertical current density. We statistically examined whether an AR is born with neutralized or non-neutralized currents, by focusing on the main phase of flux emergence, i.e., the phase in which the total unsigned magnetic flux is continuously increased. Such a large-sample statistical study suggests that most of the ARs were born with currents close to neutralization. The degree of current neutralization seems to be not affected by the AR sizes, the AR growing rate, and the AR's total unsigned current. The only systematic correlation as found is that the stronger the nonpotentiality of the magnetic field is, the further the AR deviates from current neutrality.

The rest of the paper is organized as follows: the data and method are presented in Section 2, the results are given in Section 3, and finally a summary is provided in Section 4.

2. Data and Method

We survey all the ARs with definite NOAA numbers observed by SDO from 2010 May to 2022 December, using the data product of space-weather HMI AR patches (SHARP, Bobra et al. 2014). The ARs are selected by using the following criteria (Duan et al. 2020). First, we only consider the emerging phase of the ARs, in which the flux of the ARs evolves from almost nothing on the solar surface to its peak flux. The total unsigned magnetic flux of the ARs should show a monotonically increasing trend, which means that the ARs have significant flux emergence when they were passing the solar disk. Second, we select the emerging ARs that can be clearly isolated with their surrounding fields on the photosphere, presuming that the magnetic flux emerges as isolated flux tubes that are well separated from the surrounding pre-existing fields. Third, in order to reduce the observation errors, only the duration when the ARs are located within $\pm 45^\circ$ in longitude from the Sun's central meridian are selected. According to all the above criteria, 86 events are selected, and the details of the events are listed in Table 1, including their NOAA numbers, start and end times, and the corresponding Carrington coordinates. Note that the longitude (latitude) is Carrington longitude (latitude) of the AR's center (i.e., the center of the SHARP patch) with respect to the disk center, in units of degree. We display the evolutions of all the ARs' total unsigned magnetic fluxes in the left panel of Figure 1. In general, it shows that the ARs with larger total fluxes emerge faster than the ARs with smaller total fluxes (Otsuji et al. 2011; Norton et al. 2017). The right panel of Figure 1 shows the unsigned flux normalized by the corresponding averaged value for each AR, and the horizontal axis is a normalized time, such that the starting and end time of the event is $t=0$ and $t=1$, respectively. This shows more clearly that most of the events have magnetic flux increased substantially in the studied time spans.

Table 1
NOAA Numbers, Durations, and Locations of all the Studied Flux Emerging ARs

No.	NOAA AR	Start Time	Longitude	Latitude	End Time	Longitude	Latitude
1	AR 11072	2010 May 21T08:00:06	-25.29	-13.63	2010 May 26T13:00:06	44.81	-14.24
2	AR 11076	2010 May 31T20:00:07	-6.78	-18.84	2010 Jun 04T16:00:07	44.47	-19.31
3	AR 11117	2010 Oct 26T03:59:57	4.30	18.27	2010 Oct 29T04:59:57	44.66	18.56
4	AR 11130	2010 Nov 28T07:59:53	-10.53	11.88	2010 Dec 02T09:59:53	44.58	12.39
5	AR 11141	2010 Dec 30T21:59:52	-3.05	37.20	2011 Jan 02T01:59:52	24.93	37.46
6	AR 11158	2011 Feb 12T13:59:54	-20.21	-14.39	2011 Feb 17T10:59:54	44.85	-14.17
7	AR 11327	2011 Oct 20T13:59:58	-18.73	-26.34	2011 Oct 24T00:59:57	27.38	-26.06
8	AR 11416	2012 Feb 08T13:59:53	-44.02	-11.58	2012 Feb 15T04:59:54	44.72	-11.22
9	AR 11422	2012 Feb 19T11:59:54	-9.89	22.59	2012 Feb 22T22:59:55	36.62	22.71
10	AR 11431	2012 Mar 04T11:59:56	16.26	-20.95	2012 Mar 06T15:59:56	44.67	-20.95
11	AR 11460	2012 Apr 18T01:00:02	-25.59	21.47	2012 Apr 23T00:00:03	41.11	21.04
12	AR 11551	2012 Aug 20T04:00:06	-11.20	5.26	2012 Aug 23T21:00:05	38.92	5.14
13	AR 11561	2012 Aug 30T01:00:05	-28.89	-19.08	2012 Aug 30T20:00:05	-18.18	-19.08
14	AR 11630	2012 Dec 08T11:59:53	-23.39	19.09	2012 Dec 11T09:59:52	15.65	19.47
15	AR 11640	2012 Dec 30T13:59:52	-23.17	30.84	2013 Jan 04T17:59:52	44.73	31.43
16	AR 11645	2013 Jan 02T19:59:52	-12.58	-10.24	2013 Jan 04T23:59:52	16.66	-9.98
17	AR 11682	2013 Feb 26T01:59:55	-9.25	-11.21	2013 Feb 28T23:59:55	29.82	-11.17
18	AR 11702	2013 Mar 20T18:59:58	10.00	15.09	2013 Mar 23T05:59:59	43.36	15.00
19	AR 11726	2013 Apr 19T05:00:02	-14.30	18.00	2013 Apr 23T14:00:03	44.80	17.60
20	AR 11750	2013 May 15T01:00:05	0.95	-7.33	2013 May 17T16:00:06	36.51	-7.63
21	AR 11764	2013 Jun 02T01:00:07	10.09	12.85	2013 Jun 04T00:00:07	36.56	12.61
22	AR 11765	2013 Jun 05T13:00:07	-24.40	10.51	2013 Jun 10T00:00:08	36.03	9.98
23	AR 11776	2013 Jun 20T05:00:08	12.50	9.24	2013 Jun 22T14:00:08	44.62	8.98
24	AR 11781	2013 Jun 27T21:00:08	-11.35	19.02	2013 Jul 01T00:00:08	30.25	18.66
25	AR 11784	2013 Jul 03T13:00:08	-11.31	-17.98	2013 Jul 05T00:00:08	8.33	-18.14
26	AR 11807	2013 Jul 28T11:00:08	-3.17	23.35	2013 Jul 30T12:00:08	23.58	23.20
27	AR 11813	2013 Aug 07T12:00:07	-0.32	-19.55	2013 Aug 10T00:00:07	33.42	-19.71
28	AR 11824	2013 Aug 17T11:00:06	4.51	-20.47	2013 Aug 19T17:00:06	34.87	-20.56
29	AR 11843	2013 Sep 17T08:00:03	-15.24	-6.14	2013 Sep 19T05:00:02	10.28	-6.12
30	AR 11855	2013 Sep 30T15:00:01	-20.03	-20.24	2013 Oct 04T00:00:00	25.52	-20.09
31	AR 11922	2013 Dec 10T00:59:52	5.96	9.86	2013 Dec 12T21:59:52	44.92	10.22
32	AR 11946	2014 Jan 05T15:59:52	-25.21	12.20	2014 Jan 09T23:59:52	33.55	12.69
33	AR 12003	2014 Mar 10T14:59:57	4.37	15.15	2014 Mar 13T12:59:57	44.00	15.12
34	AR 12089	2014 Jun 13T15:00:08	6.27	17.22	2014 Jun 16T12:00:08	44.81	16.87
35	AR 12119	2014 Jul 18T10:00:08	-23.26	-25.92	2014 Jul 23T00:00:08	37.78	-26.33
36	AR 12219	2014 Nov 25T12:59:54	-13.48	2.72	2014 Nov 29T19:59:53	44.89	3.24
37	AR 12234	2014 Dec 12T05:59:52	1.81	4.56	2014 Dec 14T23:59:52	39.22	4.90
38	AR 12257	2015 Jan 09T02:59:52	16.99	9.96	2015 Jan 10T19:59:52	40.20	10.13
39	AR 12273	2015 Jan 26T11:59:52	-8.98	2.86	2015 Jan 29T13:59:52	32.98	3.10
40	AR 12422	2015 Sep 24T19:00:01	-26.50	-26.83	2015 Sep 30T03:00:01	44.73	-26.63
41	AR 12530	2016 Apr 11T00:00:01	-2.54	21.03	2016 Apr 13T00:00:01	24.38	20.88
42	AR 12543	2016 May 09T06:00:05	-11.00	-2.04	2016 May 12T21:00:05	38.28	-2.42
43	AR 12571	2016 Aug 05T18:00:07	-12.30	7.86	2016 Aug 09T23:00:07	44.47	7.59
44	AR 12581	2016 Aug 29T22:00:05	19.07	5.11	2016 Aug 31T06:00:05	37.08	5.09
45	AR 12635	2017 Feb 08T16:59:53	-31.45	19.54	2017 Feb 13T08:59:54	31.55	19.79
46	AR 12673	2017 Sep 03T04:00:04	-8.37	-16.47	2017 Sep 06T06:00:04	33.44	-16.49
47	AR 12675	2017 Aug 30T23:00:05	8.50	-13.21	2017 Sep 01T11:00:05	28.88	-13.21
48	AR 12715	2018 Jun 19T11:00:08	-40.22	6.69	2018 Jun 20T22:00:08	-20.43	6.53
49	AR 12720	2018 Aug 23T21:00:05	10.78	0.83	2018 Aug 25T16:00:05	35.10	0.79
50	AR 12723	2018 Sep 29T15:00:01	-4.16	-16.11	2018 Oct 02T08:00:01	32.55	-15.98
51	AR 12733	2019 Jan 24T13:59:52	3.12	11.06	2019 Jan 26T20:59:52	34.26	11.26
52	AR 12734	2019 Mar 04T22:59:55	-40.16	16.25	2019 Mar 06T07:47:56	-21.62	16.24
53	AR 12735	2019 Mar 17T06:59:57	-41.19	9.64	2019 Mar 19T07:47:57	-13.52	9.59
54	AR 12736	2019 Mar 19T04:23:57	12.13	15.51	2019 Mar 21T13:47:57	44.58	15.43
55	AR 12757	2020 Jan 25T12:11:52	-21.06	8.27	2020 Jan 26T08:35:52	-9.50	8.35
56	AR 12772	2020 Aug 16T15:00:06	2.17	11.18	2020 Aug 18T21:24:05	32.55	11.07
57	AR 12775	2020 Oct 09T15:47:59	-27.72	-30.24	2020 Oct 11T19:47:58	0.98	-30.11
58	AR 12778	2020 Oct 25T08:11:57	-8.51	-24.18	2020 Oct 27T21:47:56	25.80	-23.96
59	AR 12806	2021 Mar 01T20:47:55	-14.08	-24.06	2021 Mar 03T17:47:55	10.33	-24.06

Table 1
(Continued)

No.	NOAA AR	Start Time	Longitude	Latitude	End Time	Longitude	Latitude
60	AR 12814	2021 Apr 10T08:00:01	-44.97	-16.39	2021 Apr 15T00:48:01	17.56	-16.73
61	AR 12827	2021 May 29T14:24:06	-44.93	13.34	2021 May 31T18:12:06	-15.78	13.09
62	AR 12832	2021 Jun 09T04:48:07	-12.44	14.74	2021 Jun 11T19:48:07	22.90	14.45
63	AR 12845	2021 Jul 17T04:36:08	-3.60	-19.74	2021 Jul 18T07:36:08	11.54	-19.84
64	AR 12850	2021 Jul 31T18:48:07	0.46	-36.85	2021 Aug 03T12:48:07	36.21	-37.04
65	AR 12873	2021 Sep 19T20:12:02	-7.47	19.20	2021 Sep 21T10:12:02	13.41	19.27
66	AR 12877	2021 Sep 27T05:48:01	4.90	-25.01	2021 Sep 30T01:48:00	42.86	-24.90
67	AR 12906	2021 Dec 13T12:11:52	-44.05	-28.81	2021 Dec 14T22:47:52	-25.20	-28.62
68	AR 12910	2021 Dec 14T15:59:52	-18.62	14.57	2021 Dec 17T19:47:51	23.99	14.97
69	AR 12929	2022 Jan 13T20:47:51	-10.00	11.44	2022 Jan 16T00:47:51	19.42	11.67
70	AR 12931	2022 Jan 13T10:47:51	20.01	16.62	2022 Jan 15T06:35:51	44.67	16.81
71	AR 12945	2022 Feb 10T11:23:53	14.71	-13.83	2022 Feb 11T14:47:53	29.95	-13.77
72	AR 12949	2022 Feb 15T04:11:53	-5.94	31.01	2022 Feb 16T15:47:53	13.69	31.06
73	AR 12964	2022 Mar 06T23:11:56	3.61	-18.18	2022 Mar 09T13:47:56	38.06	-18.21
74	AR 12972	2022 Mar 19T05:47:57	-28.53	-20.63	2022 Mar 21T08:47:58	-0.60	-20.70
75	AR 13004	2022 May 02T03:48:03	-24.63	-10.68	2022 May 03T02:48:04	-11.72	-10.78
76	AR 13008	2022 May 11T06:00:05	-44.99	19.66	2022 May 13T00:48:05	-21.04	19.48
77	AR 13026	2022 May 30T23:12:06	9.29	16.86	2022 Jun 01T23:48:06	36.52	16.61
78	AR 13027	2022 May 31T23:12:06	-16.86	-15.75	2022 Jun 01T20:24:06	-5.00	-15.85
79	AR 13065	2022 Jul 22T05:36:08	-12.34	-24.84	2022 Jul 23T14:36:07	6.05	-24.94
80	AR 13066	2022 Jul 24T12:36:07	-33.06	-21.70	2022 Jul 26T06:48:07	-9.42	-21.86
81	AR 13072	2022 Aug 04T06:12:07	18.28	-29.67	2022 Aug 05T15:48:07	36.85	-29.75
82	AR 13073	2022 Aug 04T12:24:07	23.37	-39.50	2022 Aug 04T23:48:07	29.52	-39.55
83	AR 13085	2022 Aug 20T16:48:05	-33.91	23.76	2022 Aug 22T19:48:05	-6.20	23.67
84	AR 13108	2022 Sep 20T18:48:02	-33.44	-19.99	2022 Sep 22T12:48:01	-9.81	-19.93
85	AR 13122	2022 Oct 14T13:23:58	8.11	19.84	2022 Oct 15T17:47:58	23.74	19.91
86	AR 13124	2022 Oct 14T23:47:58	15.89	-40.89	2022 Oct 17T04:47:58	44.36	-40.71

Note. The longitude is the Carrington longitude of the AR's center (i.e., the center of the SHARP patch) with respect to the disk center, in units of degree. The latitude is the Carrington latitude of the AR's center, in units of degree.

The vertical component of the current density j_z for each AR is calculated from the vector magnetogram of the SHARP data, which has a time cadence of 12 minutes and pixel size of $0''.5$. In totality, 25,477 vector magnetograms are obtained to compute the vertical current density and then the degree of current neutralization with all the ARs considered. j_z is calculated according to Ampère's Law:

$$j_z = \frac{1}{\mu_0} \left(\frac{\partial B_y}{\partial x} - \frac{\partial B_x}{\partial y} \right). \quad (1)$$

A central finite difference scheme is used to obtain the derivatives. The finite difference scheme may give false signals, such as large random values, when the small-scale structures and data noise exist in the vector magnetograms. In order to reduce the impact of this randomly generated current density, we apply smoothing in time to the raw value of j_z with a window of 2 hr. In addition, the fields with strength below 220 G are generally considered to be noisy (Bobra et al. 2014). Thus, to avoid data with a low signal-to-noise ratio, only j_z in the regions with magnetic field strength above 220 G are used in our analysis.

In theory, the positive and negative fluxes should be balanced strictly with each other for isolated ARs. For the data, the degree of flux balance can be quantified as

$$e_{\text{flux}} = \frac{|\Phi_n|}{\Phi_u} = \frac{\left| \int B_z dx dy \right|}{\int |B_z| dx dy}, \quad (2)$$

where Φ_n is the net flux, Φ_u the total unsigned flux. In the left panel of Figure 2, we show the values for all the events. One can see that most of the events have $e_{\text{flux}} < 0.1$, indicating a high degree of flux balance. In addition, for a current-carrying isolated AR, the total current also should be balanced, which can be similarly quantified as

$$e_{\text{current}} = \frac{|I_n|}{I_u} = \frac{\left| \int j_z dx dy \right|}{\int |j_z| dx dy}. \quad (3)$$

As shown in the right panel of Figure 2, most of the events have $e_{\text{current}} < 0.1$, indicating a high degree of the current balance.

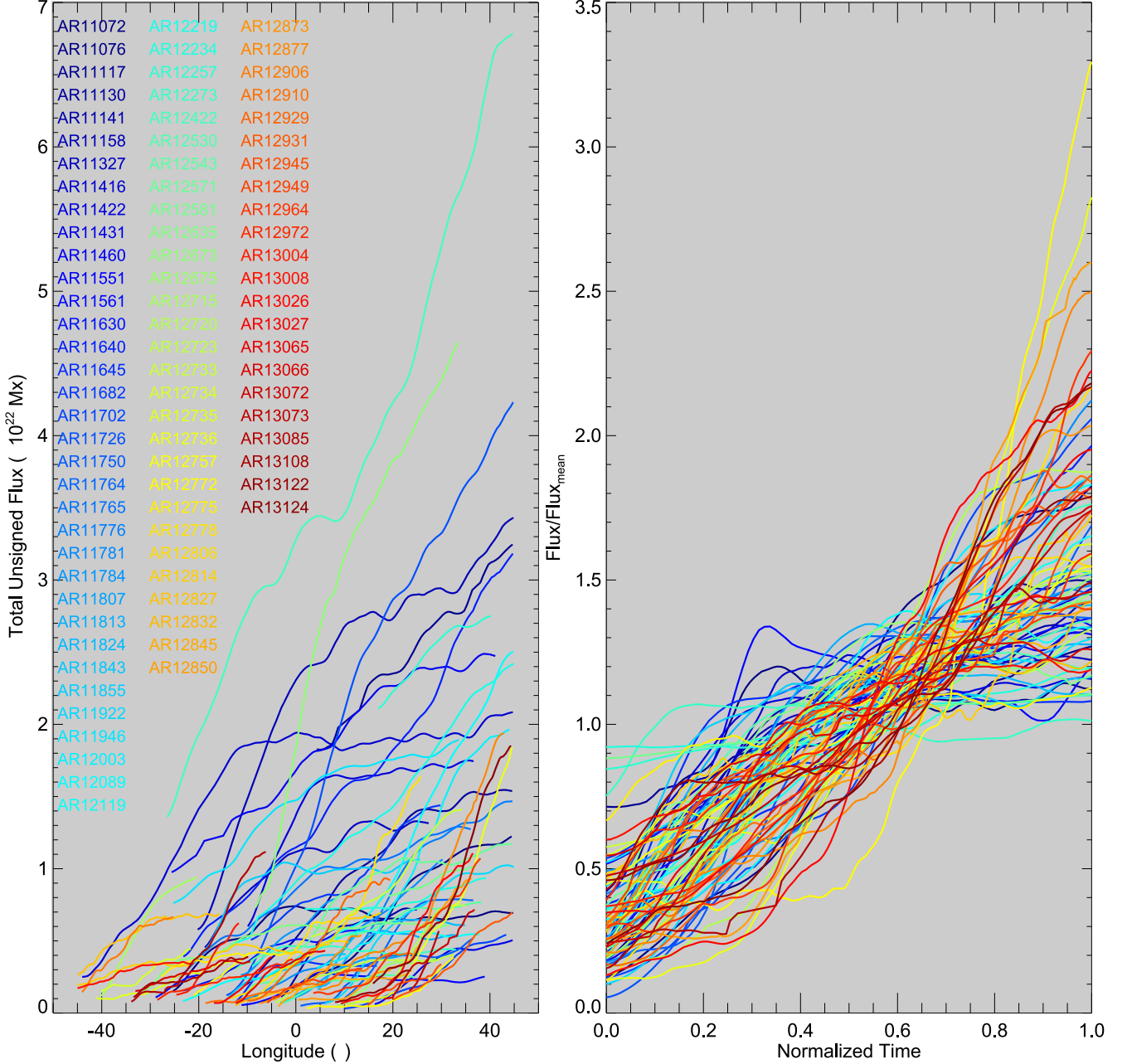


Figure 1. Evolution of the total unsigned magnetic flux for all the selected 86 flux emerging ARs. In the left panel, the horizontal axis is the AR center's longitude relative to the solar disk center, serving as an indicator of the temporal evolution. Note that the selected events fall within a longitude range of -45° to 45° . The colors of curves denote the NOAA number of the ARs. In the right panel, the unsigned flux is normalized by the corresponding averaged value for each AR, and the horizontal axis is a normalized time, such that the starting and end time of the event is $t = 0$ and $t = 1$, respectively.

Then, we use $I_{s,0}^{+,-}$ to denote four different currents, which are integrated from j_z as

$$I_{s,0}^{+,-} = \int_{B_z^{+,-}} j_z^{s,0} dx dy, \quad (4)$$

where B_z^+ and B_z^- denote the positive and negative magnetic polarities, respectively, and j_z^s and j_z^o denote the current density

that has the same and opposite sign with the corresponding B_z . For a current-neutralized field,

$$I_s^+ + I_0^+ = I_s^- + I_0^- = 0. \quad (5)$$

Generally, the DC (RC) does not necessarily have the same (opposite) sign with B_z , and in this paper we simply considered

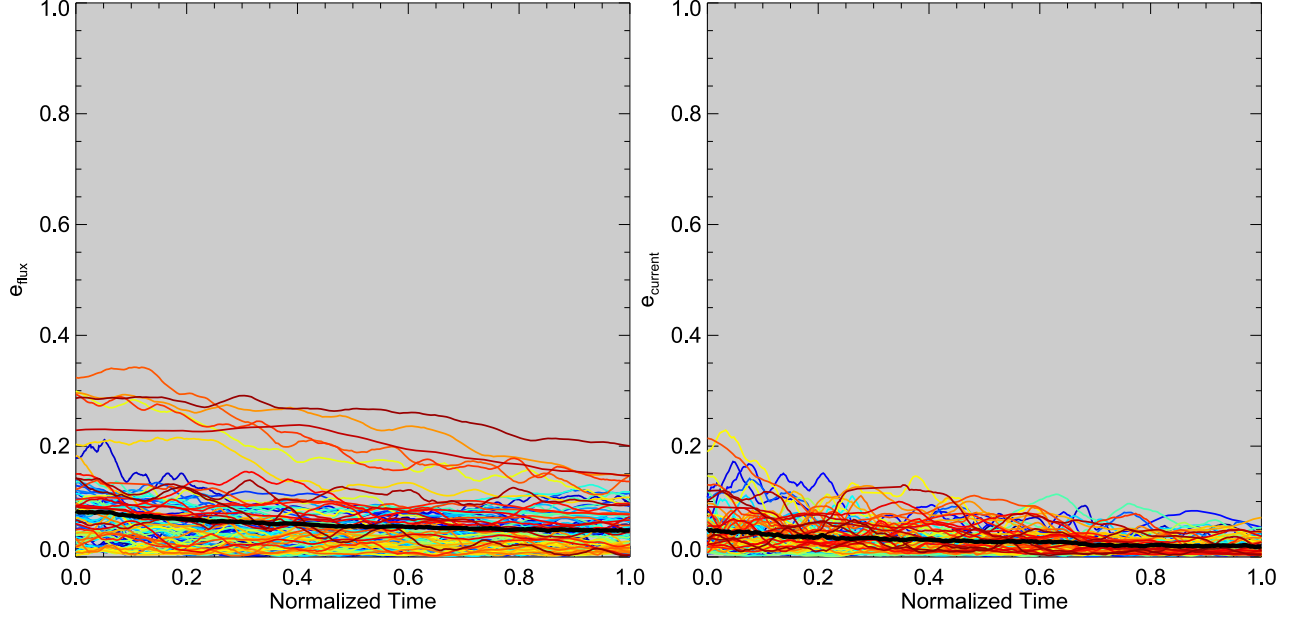


Figure 2. Evolutions of the total flux balance degree e_{flux} and total current balance degree e_{current} for all the selected 86 flux emerging ARs. The horizontal axis is a normalized time, such that the starting and end time of the event is $t = 0$ and $t = 1$, respectively. The colors of the curves denote the NOAA number of the ARs, as shown in Figure 1. The thick, black curves show the average values for all the ARs.

that DC is the dominant current in each polarity. Specifically, in the positive (negative) polarity, the direct current DC^+ (DC^-) is the one with the larger magnitude among the two currents $I_{s, o}^+$ ($I_{s, o}^-$), and RC^+ (RC^-) is the remaining one, namely,

$$(\text{DC}^\pm, \text{RC}^\pm) = \begin{cases} (I_s^\pm, I_o^\pm); & \text{if } |I_s^\pm| \geq |I_o^\pm|, \\ (I_o^\pm, I_s^\pm); & \text{if } |I_s^\pm| < |I_o^\pm|. \end{cases} \quad (6)$$

We note that such a simple distinction of DC and RC may not be universally correct, but will not affect the result of our study, since here we only care about the degree of neutralization, there is no need to discriminate whether DC follows along or inverse to the magnetic field.

The degree of current neutralization for the magnetic field with positive and negative B_z , as well as for the entire AR was measured by three ratios of currents:

$$|\text{DC}/\text{RC}|^+ = |\text{DC}^+|/|\text{RC}^+|, \quad (7)$$

$$|\text{DC}/\text{RC}|^- = |\text{DC}^-|/|\text{RC}^-|, \quad (8)$$

and

$$|\text{DC}/\text{RC}| = \frac{|\text{DC}^+| + |\text{DC}^-|}{|\text{RC}^+| + |\text{RC}^-|}, \quad (9)$$

which is an average value for all polarities. For a perfect magnetogram with flux balanced exactly and free of noises, the three ratios should be equal to one another. For a current-neutralized field, these ratios will be identical to unity, and any non-neutralized current will have all these ratios above unity.

3. Results

Before analyzing the statistical results, we show the results for two well-studied, flare-productive ARs in the literature, NOAA 11158 and 12673, in Figure 3. The unsigned flux of both ARs increase significantly, with the average emerging rate of $2.5 \times 10^{20} \text{ Mx hr}^{-1}$ and $5.5 \times 10^{20} \text{ Mx hr}^{-1}$, respectively. Furthermore, during their emerging phase, both the ARs have flux balanced well, with $e_{\text{flux}} \sim 0.02$ for AR 11158 and $e_{\text{flux}} \sim 0.04$ for AR 12673 (not shown in the figure). In AR 11158, the current ratios for the positive polarity ($|\text{DC}/\text{RC}|^+$), the negative polarity ($|\text{DC}/\text{RC}|^-$) and the whole AR ($|\text{DC}/\text{RC}|$) varies between 1.0 and 1.8, with an average value of around 1.45. Note that there are small differences between the three ratios due to non-perfection of flux and current balances. For AR 12673, the current neutralization degrees are between 1.1 and 2.5; with an average of around 1.8. Therefore, in both ARs, the currents deviate from neutralization clearly in most of the emerging phase, in agreement with some previous studies (Avallone & Sun 2020).

Two typical flux-emergence MHD simulations, which are obtained from Toriumi & Takasao (2017) and Syntelis et al. (2017), respectively, are taken as a comparison with the observations. Both the two simulations aim to reproduce the birth of an AR with significant nonpotentiality. Initially, an isolated, twisted flux tube is placed in the convection zone. With the aid of buoyant force, the flux tube rises to the photosphere, and then emerges into the corona. In the simulations, the magnetic field at the photospheric height is

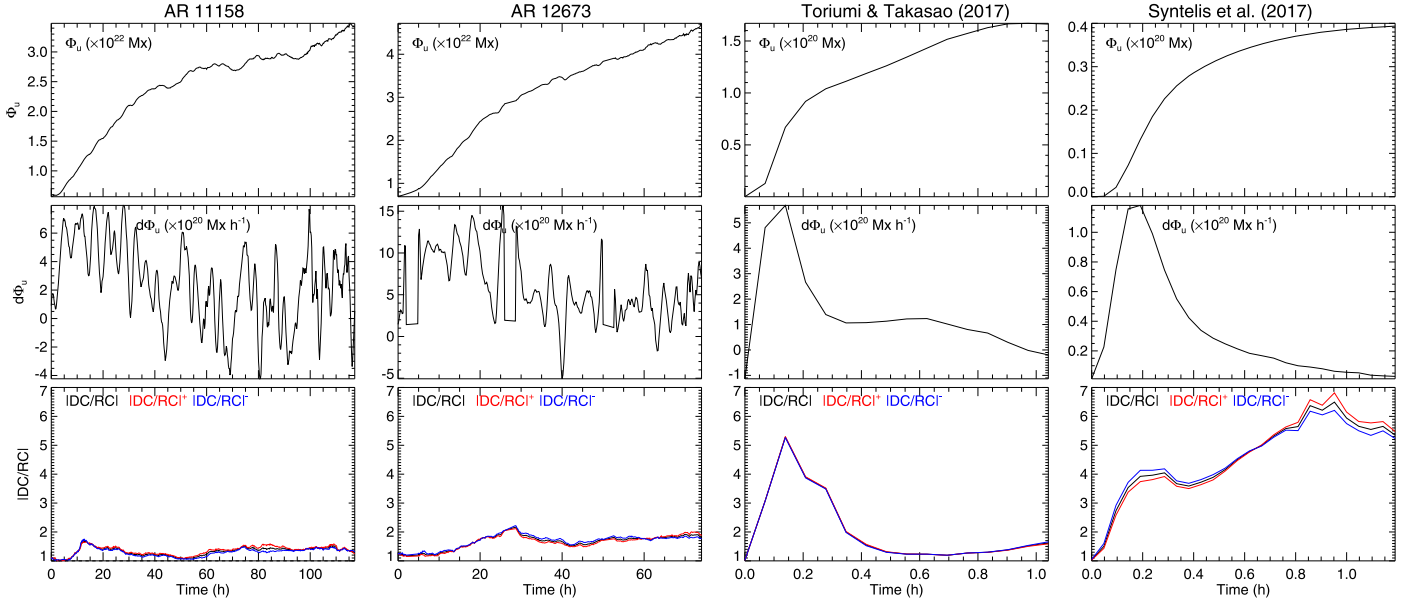


Figure 3. Comparison of different parameters between two flux-emerging ARs from observation and that from numerical simulations. From top to bottom are the evolution of total unsigned flux, flux emergence rate, and the degree of current neutralization. The results are shown for ARs 11158 and 12673, as well as simulations by Toriumi & Takasao (2017) and Syntelis et al. (2017), respectively. For the simulations, results for the height of $z_0 = 0.14$ Mm in Toriumi & Takasao (2017) simulation and $z_0 = 0.12$ Mm in Syntelis et al. (2017) simulation are shown. The horizontal axes represent time for various events.

used to compute the current density. Comparing the simulations with the observed ones, we find the flux contents in the simulations are smaller by two orders of magnitude, but the peak flux-emergence rates are on the same order. Unlike a steady increase for several days in the two ARs, the flux in both simulations show a fast rising and saturation in about an hour. The current is much more strongly non-neutralized in the simulations. In Toriumi & Takasao (2017), the ratio of DC to RC first quickly increases to a large value of about 5 with the fast flux emergence, indicating that the current neutralization is strongly destroyed. The ratio then decreases with the slowing down of the emergence to a small value of around 1.5 until the saturation of the flux. Similarly, in Syntelis et al. (2017) the ratio also rises quickly in the early phase, but it keeps rising overall with the slowing down of the emergence, and attains a higher value of around 6 when the flux saturated. Note that even in these simulations which are free of noises, there are still small differences between three current ratios (i.e., $|\text{DC}/\text{RC}|^+$, $|\text{DC}/\text{RC}|^-$, $|\text{DC}/\text{RC}|$) for the same simulation.

Figure 4 shows the evolutions of the current ratios for all the ARs. Overall, we find that the ratios are close to unity, with an average profile of around 1.2, which has no systematic relation with the normalized time. This suggests that for the majority of the flux-emerging ARs, the photospheric currents are close to being neutralized, and do not evolve with the continuous injection of magnetic flux. Figure 5 further shows the histograms of the current ratios for all the 25477 magnetograms, with both the average and median values denoted. As

can be expected, all of them are clustered close to unity, with an average value of around 1.2, and a median value of 1.1. These results suggest that, in statistical sense, the photospheric fields of ARs are actually not far from the current neutralization during the flux-emerging phase.

We further explore whether the current ratios are correlated to some specific parameters of the field. In Figure 6, we display the two-dimensional histograms between the degree of neutralization and a sequence of parameters, respectively. They include the total unsigned magnetic flux Φ_u , the flux changing rate $d\Phi_u/dt$, the total unsigned current I_u , and the nonpotentiality which is quantified by the average twist parameter α_{tot} (Bobra et al. 2014) defined as

$$\alpha_{\text{tot}} = \frac{\int j_z B_z dx dy}{\int B_z^2 dx dy}. \quad (10)$$

The distributions of frequency are shown by the colors in the two-parameter spaces. As the results for $|\text{DC}/\text{RC}|^+$ and $|\text{DC}/\text{RC}|^-$ are almost identical to $|\text{DC}/\text{RC}|$, here we only show that of $|\text{DC}/\text{RC}|$. The Spearman rank correlations between the current ratio with the different parameters are calculated. As can be seen, there is no systematic correlation between the ratio $|\text{DC}/\text{RC}|$ and either the total unsigned magnetic flux or the emergence rates, as the correlation coefficients (CCs) of $|\text{DC}/\text{RC}|$ and these two parameters are less than 0.2. Also, no correlation is not found between $|\text{DC}/\text{RC}|$ and the total unsigned current. The only significant correlation exists

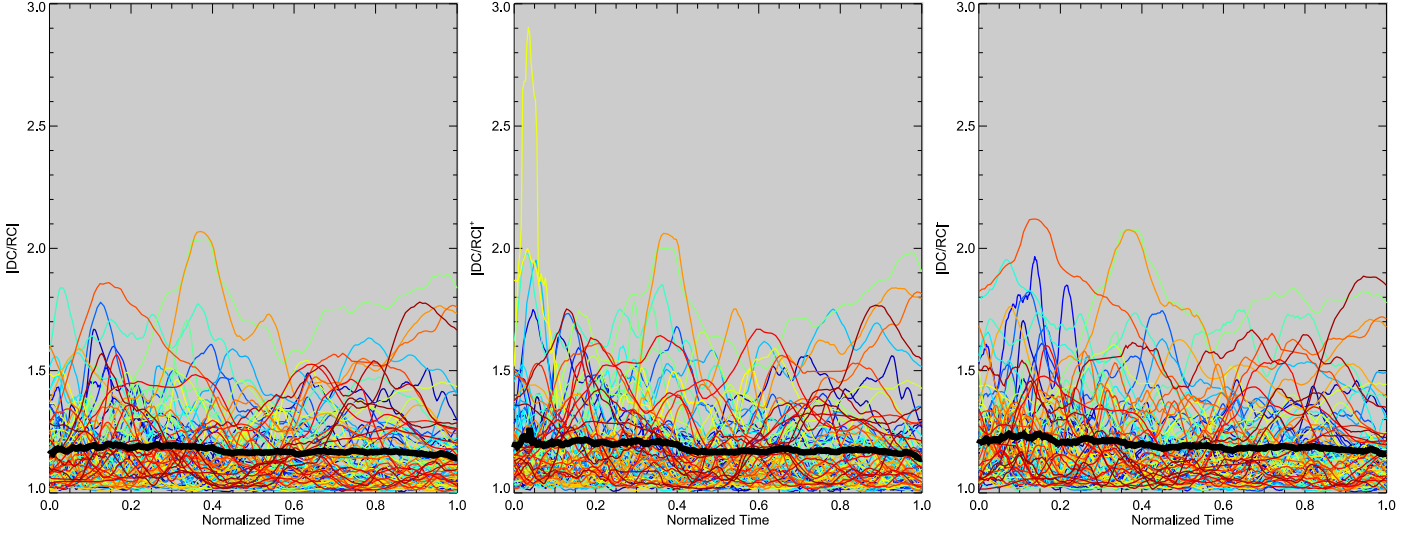


Figure 4. Evolution of $|\text{DC}/\text{RC}|$, $|\text{DC}/\text{RC}|^+$, and $|\text{DC}/\text{RC}|^-$ for all the ARs. The horizontal axis is the normalized time. The colors of curves denote the NOAA number of the ARs as shown in Figure 1. The thick, black curves show the average values for all the ARs.

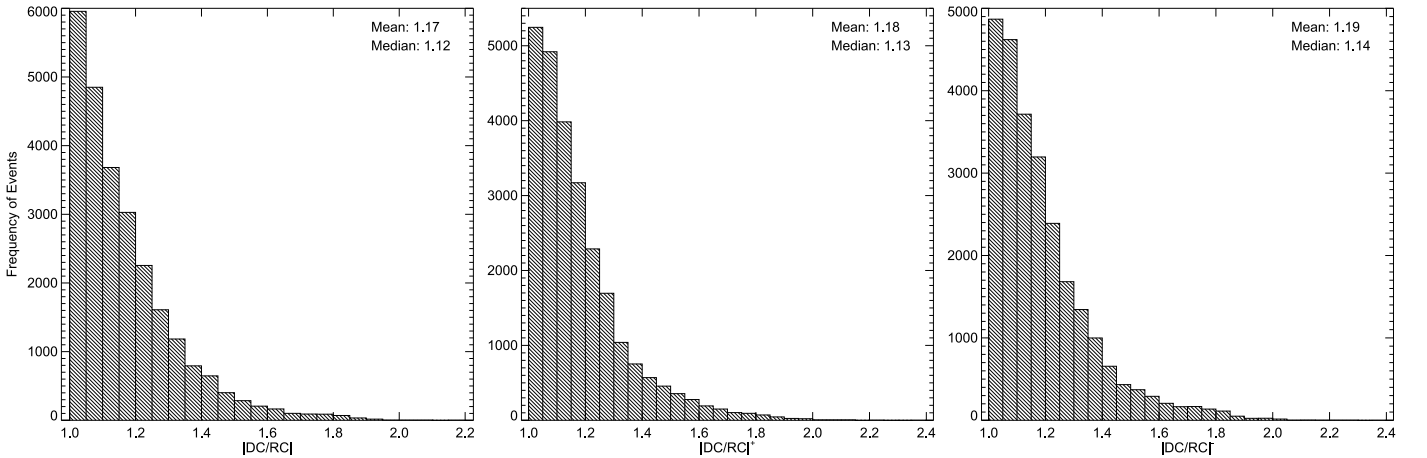


Figure 5. Histogram distributions for $|\text{DC}/\text{RC}|$, $|\text{DC}/\text{RC}|^+$, and $|\text{DC}/\text{RC}|^-$ for all the 25477 magnetograms across all the analyzed ARs.

between $|\text{DC}/\text{RC}|$ and the nonpotentiality α_{tot} , which has a CC of 0.7.

4. Summary

In this paper, we have conducted a systematic survey of the degree of current neutralization in flux-emerging ARs based on the vector magnetograms obtained from SDO/HMI. The sample consists of all the well-isolated, flux-emerging ARs on the solar disk with definite NOAA numbers from 2010 May to 2022 December. The statistical results suggest that most of the ARs are born with currents close to neutralization, with the ratio of DC to RC around $1.1 \sim 1.2$, and there are very few cases with the ratio larger than 2.0. We also analyzed two typical numerical simulations of flux emergence, and found

that they produced much larger values of $|\text{DC}/\text{RC}|$ than those from the observations.

It appears that there is no correlation between the ratio $|\text{DC}/\text{RC}|$ and the AR sizes as measured by total unsigned magnetic flux, the AR growing rate as measured by the increasing rate of the unsigned flux, and the AR's total unsigned current. Notably, the only systematic correlation is identified between $|\text{DC}/\text{RC}|$ degrees and the overall nonpotentiality of the fields. Specifically, the stronger the nonpotentiality of the magnetic field, the further the AR deviates from current neutrality. Since the stronger the nonpotentiality of an AR is, the more likely it is to generate solar eruptions, our result is consistent with previous findings (Liu et al. 2017; Vemareddy 2019; Avallone & Sun 2020), which proposed a positive relationship between

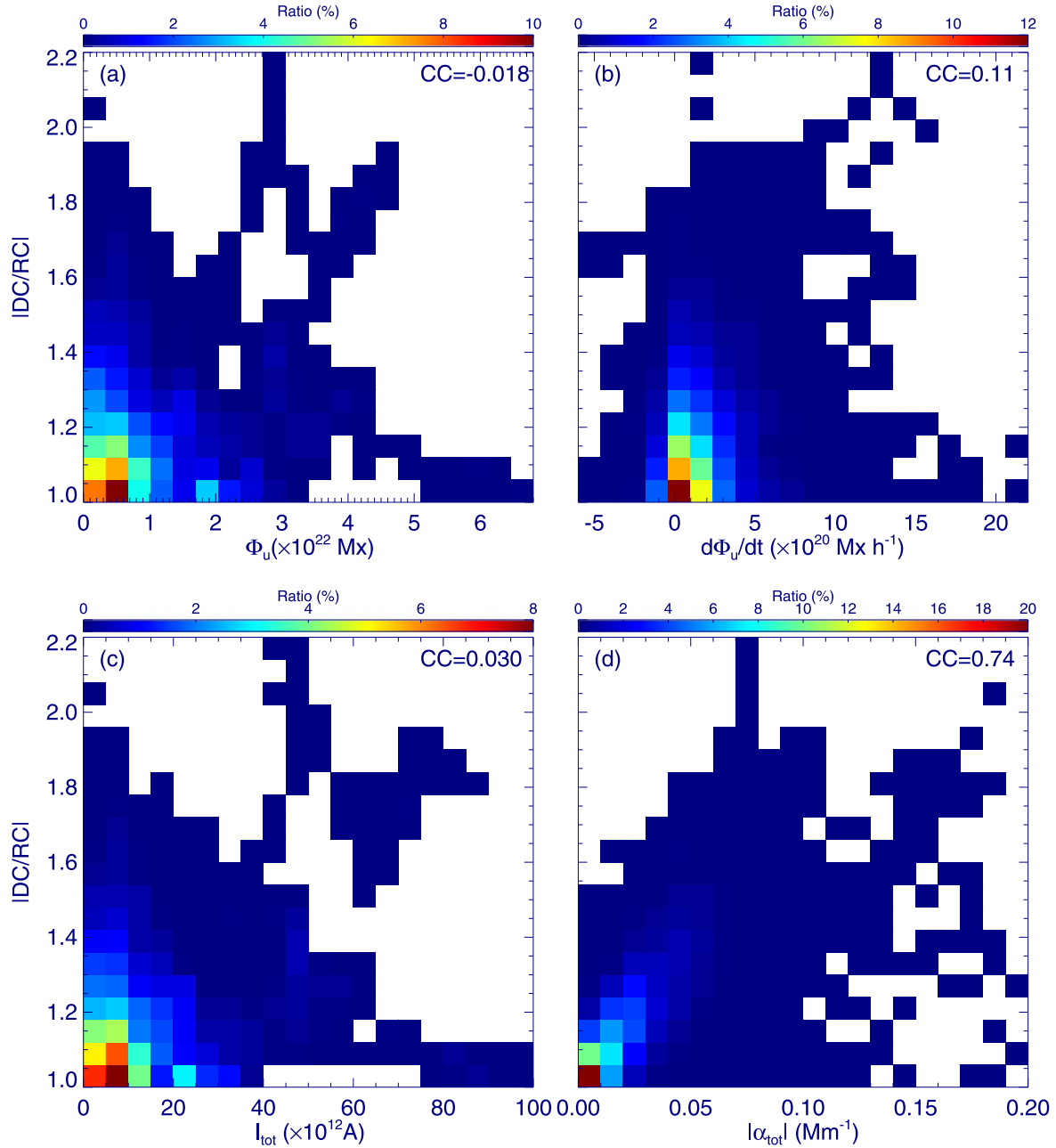


Figure 6. 2D histograms in spaces spanned by $|\text{DC}/\text{RC}|$ and different parameters, including the total unsigned flux Φ_u (a), the flux changing rate $d\Phi_u/dt$ (b), the total unsigned current I_{tot} (c), and the mean twist parameter α_{tot} (d). The colors indicate the frequency (in percent) of events in a specific bin. The correlation coefficients (CCs) between $|\text{DC}/\text{RC}|$ with the different parameters are denoted in each panel.

the flare/CME activity of an AR and its degree of current non-neutralization.

Acknowledgments

This work is supported by the National Natural Science Foundation of China (NSFC) U2031108 and Yunnan Key Laboratory of Solar Physics and Space Science under the

number YNSPCC202213. Data from observations are courtesy of NASA/SDO. We thank Shin Toriumi and Petros Syntelis for sharing the data of the flux emergence simulations.

References

- Aulanier, G., Török, T., Démoulin, P., & DeLuca, E. E. 2010, *ApJ*, 708, 314
 Avallone, E. A., & Sun, X. 2020, *ApJ*, 893, 123
 Bobra, M. G., Sun, X., Hoeksema, J. T., et al. 2014, *SoPh*, 289, 3549

- Duan, A., Jiang, C., Toriumi, S., & Syntelis, P. 2020, *ApJL*, 896, L9
- Fursyak, Y. A., Kutsenko, A. S., & Abramenko, V. I. 2020, *SoPh*, 295, 19
- Georgoulis, M. K., Titov, V. S., & Mikić, Z. 2012, *ApJ*, 761, 61
- Hoeksema, J. T., Liu, Y., Hayashi, K., et al. 2014, *SoPh*, 289, 3483
- Kliem, B., & Török, T. 2006, *PhRvL*, 96, 255002
- Kontogiannis, I., Georgoulis, M. K., Park, S.-H., & Guerra, J. A. 2017, *SoPh*, 292, 159
- Leka, K. D., Canfield, R. C., McClymont, A. N., & van Driel-Gesztelyi, L. 1996, *ApJ*, 462, 547
- Liu, Y., Sun, X., Török, T., Titov, V. S., & Leake, J. E. 2017, *ApJL*, 846, L6
- Longcope, D. W., & Welsch, B. T. 2000, *ApJ*, 545, 1089
- Manchester, W. B., IV, Vourlidas, A., Tóth, G., et al. 2008, *ApJ*, 684, 1448
- Melrose, D. B. 1991, *ApJ*, 381, 306
- Melrose, D. B. 1995, *ApJ*, 451, 391
- Norton, A. A., Jones, E. H., Linton, M. G., & Leake, J. E. 2017, *ApJ*, 842, 3
- Otsuji, K., Kitai, R., Ichimoto, K., & Shibata, K. 2011, *PASJ*, 63, 1047
- Parker, E. N. 1979, *Cosmical Magnetic Fields. Their Origin and their Activity* (Oxford: Oxford Univ. Press)
- Parker, E. N. 1996, *ApJ*, 471, 485
- Pesnell, W. D., Thompson, B. J., & Chamberlin, P. C. 2012, *SoPh*, 275, 3
- Ravindra, B., Venkatakrishnan, P., Tiwari, S. K., & Bhattacharyya, R. 2011, *ApJ*, 740, 19
- Schrijver, C. J., De Rosa, M. L., Title, A. M., & Metcalf, T. R. 2005, *ApJ*, 628, 501
- Syntelis, P., Archontis, V., & Tsinganos, K. 2017, *ApJ*, 850, 95
- Toriumi, S., & Takasao, S. 2017, *ApJ*, 850, 39
- Toriumi, S., & Wang, H. 2019, *LRSP*, 16, 3
- Török, T., & Kliem, B. 2005, *ApJL*, 630, L97
- Török, T., Kliem, B., & Titov, V. S. 2004, *A&A*, 413, L27
- Török, T., Leake, J. E., Titov, V. S., et al. 2014, *ApJL*, 782, L10
- van Ballegoijen, A. A. 2004, *ApJ*, 612, 519
- Vemareddy, P. 2019, *MNRAS*, 486, 4936
- Vemareddy, P., Venkatakrishnan, P., & Karthikreddy, S. 2015, *RAA*, 15, 1547
- Venkatakrishnan, P., & Tiwari, S. K. 2009, *ApJL*, 706, L114
- Wheatland, M. S. 2000, *ApJ*, 532, 616
- Wilkinson, L. K., Emslie, A. G., & Gary, G. A. 1992, *ApJL*, 392, L39